Energy Engineering

Tech Science Press

https://doi.org/10.32604/ee.2026.075509

ARTICLE

Lightweight Prediction-Driven Rolling Scheduling for Off-Grid Construction Microgrids under Variable Electric Demand

Lei Shen[1,2], Qiang Gao[1], Shanyun Gu[1], Wei Li[1], Jun Li[1], Jianquan Li[1], Ruyi Xia[1] and Jie Ji[2,*]

[1]Huaian Hongneng Group Co., Ltd., Huaian, China
[2]Electric Engineering Department, Huaiyin Institute of Technology, Huaiyin, China

*Corresponding Author: Jie Ji. Email: jijie@hyit.edu.cn

Received: 03 November 2025; Accepted: 29 January 2026; Published: 30 August 2026

ABSTRACT: Aiming at the contradiction between green energy consumption and diesel dependence in temporary construction camps under the condition of "weak data-weak communication", this paper puts forward a collaborative framework of off-grid light storage and firewood storage with tight coupling of "prediction-scheduling". The prediction layer constructs a lightweight IOOA-CNN-BiLSTM-Markov model: CNN extracts the spatial characteristics of tower crane shadow and cloud cluster, BiLSTM captures the bidirectional time series dependence, Markov residual compensates the non-stationary disturbance, and uses the improved Osprey algorithm to complete the small sample superparameter self-tuning at the edge of ARM, thus realizing the error-oriented compression in the scene of lack of weather channels. The scheduling layer is designed to improve the affine adjustable rolling optimization driven by the snake optimization ISO. With the prediction interval-scene dual mode as the input, the start-stop frequency of diesel and the energy storage SOC are modeled as integer-continuous variables synchronously, and the three-objective MILP of "minimum diesel + minimum load loss + minimum light rejection" is solved in seconds, thus achieving the multi-objective coordination of green power priority, energy storage arbitrage and diesel compensation. By building a photovoltaic, energy storage and diesel hardware-in-the-loop platform and loading a typical temporary site with an impact load of 80–400 kW, the system verifies the adaptability and deployment of the proposed framework under the extreme conditions of "zero power grid, zero history and weak sensing".

KEYWORDS: Temporary construction; off-grid microgrid; photovoltaic prediction; improved osprey algorithm; improved snake optimization; rolling scheduling

1 Introduction

Under the background of the national "double carbon" strategy, transforming the energy structure in the construction industry has become a key link to realizing green and low-carbon development. This is especially critical in temporary construction scenarios without power grid coverage, such as emergency repairs after disasters, remote road construction, and military engineering projects. Traditional power supply modes relying on diesel generators not only consume high energy and produce large emissions, but also face challenges like difficult fuel transportation and high operating costs [1,2]. Therefore, building an off-grid hybrid energy system with photovoltaic power generation as the core, combined with energy storage and diesel backup, has become an important path to increase the proportion of green energy at construction sites and achieve low-carbon operations.

However, the hybrid system of light storage and diesel works well in grid-connected scenarios but fails frequently when deployed at temporary construction camps. Construction loads are mainly impacted by welding machines, tower cranes, and pump trucks, with random start-stop patterns that cause the traditional "steady load" assumption to fail instantly [3,4]. On the photovoltaic side, due to the alternating influence of tower crane shadows, cloud transients, and dust, the output fluctuates violently. Additionally, there is no long-term weather station on site, the resolution of satellite data is greater than or equal to 1 km with delays of at least 30 min, and the prediction error is 10 to 30 percent higher than in cities [5,6]. Camps usually have no public network or optical fiber, and the edge controller only has ARM-level computing power, which is directly paralyzed by high-precision prediction or GPU algorithms. How to maximize green electricity, minimize diesel consumption, and optimize cost using only "weak data plus weak communication" has become the core problem for off-grid construction scenarios.

The forecasting link bears the brunt of this challenge. Almost all existing deep models are designed for grid-connected power stations, and they immediately become unstable when faced with the "small sample, strong fluctuation, and zero redundancy" camp environment. For example, CEEMDAN-RMSE-AM-TCN-BiLSTM shows a sudden increase of 62 percent when the sample size is less than two weeks [7]. CNN-Transformer lacks cloud cover and wind speed fields, causing attention mismatch and error amplification [8]. DDPM increases sample processing time to 8 min and requires GPU resources that are out of reach for ARM terminals [4]. Once the SGMD-KPCA-PSO-BiLSTM offline decomposition base encounters dust-rain alternation, the IMF drifts and requires retraining for 3 h, making it impossible to be "plug and play" [9]. CNN-BiLSTM-Attention depends on load autocorrelation, and the random start and stop of tower cranes leads to attention homogenization, with accuracy dropping by 22 percent [3]. When MCQRNN-GAQ lacks 30-day complete samples, the quantile crosses and the interval expands, making it unusable for scheduling [6]. Transformer-BiLSTM with 10 percent sensor disconnection shows RMSE increases of 40 percent [10]. After removing the zero power at night by Bi-LSTM, a "false valley" appears in the sunrise section, and the error rises to 18 percent [11]. LLaMA-13B parameters require 48 GB of video memory, which is completely contrary to "lightweight" requirements [12]. To sum up, the approach of large models plus large samples plus high computational power is difficult to deploy in temporary camps, making it urgent to adopt a lightweight forecasting strategy for edge deployment and non-stationary series.

The dispatching link also falls into the trap of "three highs" (high accuracy dependence, high communication bandwidth, and high computational power). Existing literature assumes "accurate predictions from days ago, sufficient communication bandwidth, and sufficient computing power," which becomes completely invalid when transplanted to camps. In the multi-energy collaborative model of rural virtual power plants, the thermoelectric ratio exceeds limits under small samples of 5 min, rolling corrections increase from 2 to 11 times, and gateway delays exceed 500 ms [13]. After introducing RoCoF constraints into the water-wind-light CSP system, it becomes necessary to advance the true value of node-level photovoltaic by 15 min, but sites only have single-point irradiance sensors without cloud cover data, causing prediction error to rise from 4.8 to 18.7 percent, with insufficient frequency modulation capacity of hydropower and daily fuel consumption of diesel hot standby increasing by 12 percent [14]. The double-layer scheduling of photovoltaic-energy storage-charging stations depends on 10-min predictions, and when deviation exceeds 15 percent, the relaxation multiplier diverges and solution time extends from 3 to 47 s, causing real-time collapse [15]. The joint probability of hydrogen production from off-grid wind-solar is given by LSTM-QR-Copula, requiring 90 days of training; under one-week data, Copula mismatch causes extreme misjudgment rates to increase from 5 to 28 percent, with the electrolyzer starting and stopping frequently and diesel starting 6 times, completely offsetting low-carbon benefits [16]. Event-triggered MPC can prolong battery life by 13 percent through SOH considerations, but the threshold depends on PV curve smoothness; under load impacts, optimization frequency increases from 6 to 27 times, the edge CPU becomes fully loaded, packet loss rates rise to 8 percent, and instruction delays appear [17]. P-robust optimization uses 200 groups of Monte Carlo scenario trees to balance economy and robustness, but the weight of worst scenarios is underestimated after dust events, increasing diesel for island operation by 18 percent and raising carbon emissions [18]. The annual profit of multi-scale dispatching of electricity-hydrogen shared energy storage is 9.8 percent, but requires annual PV curves in the seasonal layer, where Shapley values cannot be calibrated with one-week data, causing the electrolyzer to run at constant power and green electricity utilization to drop from 92 to 74 percent, with diesel power supply increasing sharply [19]. Overall, existing scheduling frameworks share common problems such as over-reliance on accuracy, lack of real-time performance, and poor robustness for the "short period, weak prediction, and high uncertainty" camp environment. A new paradigm with small samples, light weight, and high fault tolerance is urgently needed to achieve the goal of supplying off-grid construction with maximum green energy, minimum diesel, and lowest cost.

Aiming at the contradiction between green energy consumption and diesel dependence in off-grid construction camps under "weak data-weak communication" conditions, this paper proposes a tightly coupled "prediction-scheduling" framework. The schematic diagram of the framework is shown in Fig. 1. Taking construction impact loads and tower crane shadow disturbances as boundaries, we construct a lightweight IOOA-CNN-BiLSTM-Markov photovoltaic prediction model that achieves error-oriented compression in small-sample, non-stationary, and channel-lacking scenarios at ARM edge. The forecast interval is then embedded into an affine adjustable rolling optimization framework, and the improved snake optimization algorithm (ISO) solves the mixed-integer linear programming problem with objectives of minimum diesel plus minimum load loss. The start-stop frequency of diesel generators and energy storage SOC are simultaneously modeled as integer-continuous variables, completing the multi-objective coordination of green power priority, energy storage arbitrage, and diesel compensation within seconds. Verification under impact loads of 80 to 400 kW shows that the proposed framework reduces diesel consumption by 18 to 25 percent, increases green electricity penetration by 12 percent, and maintains load loss rates of less than 0.1 percent, confirming the engineering feasibility of the small-sample, lightweight, high-fault-tolerant approach.

2 System Operating Framework

2.1 IOOA-CNN-BiLSTM-Markov Prediction Model

2.1.1 Convolutional Neural Networks (CNN)

Convolutional Neural Networks can be trained using both supervised and unsupervised learning approaches [20], enabling them to effectively learn patterns and features from data across different application scenarios. As illustrated in Fig. 2, a typical CNN architecture consists of an input layer, convolutional layers, pooling layers, fully connected layers, and an output layer. The convolutional layer serves as the core component and plays a pivotal role in feature extraction. It performs linear transformations on input data to extract features from raw data, with its computational formula expressed as follows:

$$O_1 = f\ W_1^{*} I + b_1 \tag{1}$$

In the formula: O_1 represents the extracted features; W_1 and b_1 denote the weights and biases of the I-th convolutional layer, respectively; * indicates the convolution operation; f is the activation function, typically selected as the Rectified Linear Unit.

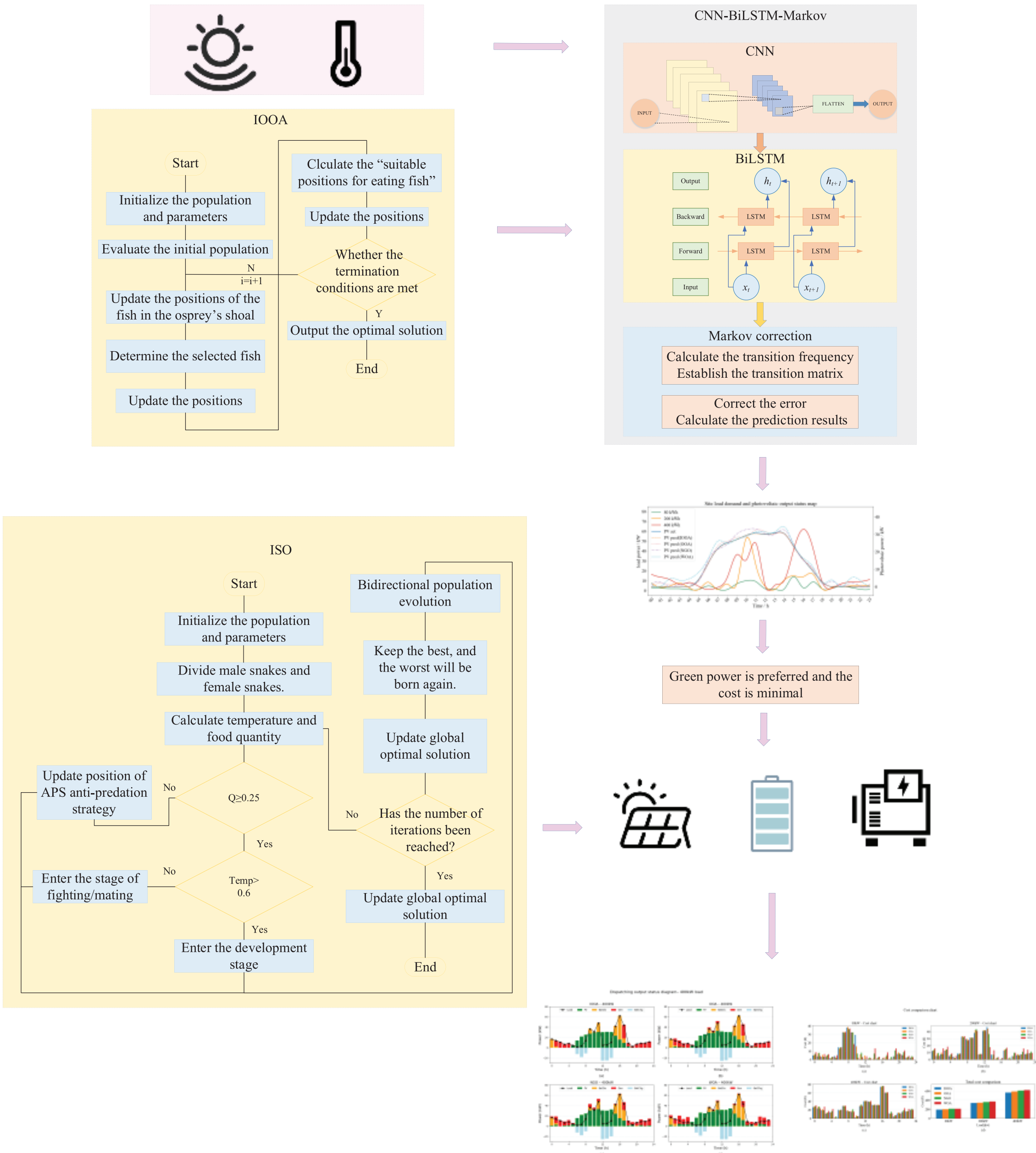

Figure 1: System framework diagram.

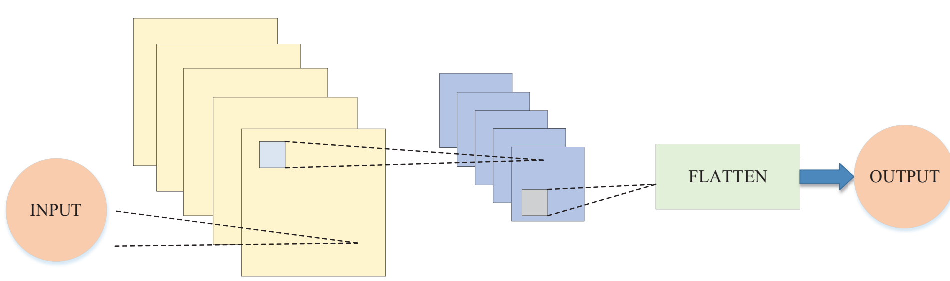

Figure 2: CNN structure diagram.

2.1.2 Bidirectional Long Short-Term Memory (BiLSTM)

Long Short-Term Memory neural networks are an improved variant of Recurrent Neural Networks (RNN) that demonstrate exceptional performance in time series prediction [21]. This study incorporates Bidirectional Long Short-Term Memory networks, which primarily consist of forward LSTM and backward LSTM components as illustrated in Fig. 3. By incorporating reverse LSTM layers, BiLSTM can effectively learn from both past and future sequence data. The computational formulas are as follows:

$$\overrightarrow{h_t} = LSTM\left(x_t, \overrightarrow{h_{t-1}}\right) \tag{2}$$

$$\overleftarrow{h_t} = LSTM\left(x_t, \overleftarrow{h_{t-1}}\right) \tag{3}$$

$$y_t = \overrightarrow{W}\overrightarrow{h_t} + \overleftarrow{W}\overleftarrow{h_t} + b_y \tag{4}$$

In the formula: $\overrightarrow{h_t}$ represents the forward LSTM hidden state at time step t, capturing past temporal dependencies of PV power; x_t denotes the current state's construction worker posture data; $\overleftarrow{h_t}$ represents the reverse LSTM hidden state at time step t; $\overrightarrow{h_{t-1}}$ and $\overleftarrow{h_{t-1}}$ are the respective previous time-step hidden states; y_t is the final BiLSTM output that concatenates both directional representations; $\overrightarrow{W}$ stands for the forward weight matrix; $\overleftarrow{W}$ represents the backward weight matrix; b_y is the offset of the linear relationship.

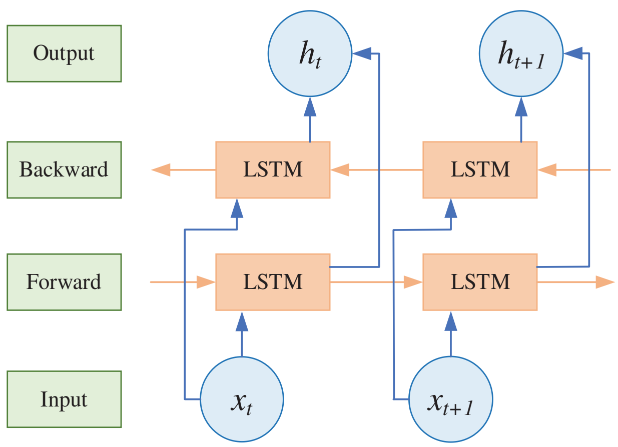

Figure 3: BiLSTM structure.

2.1.3 Markov Corrected

The Markov model is a probability-based mathematical framework that describes stochastic transition processes between different system states. Its defining characteristic is that the next state of the system depends solely on the current state, independent of any previous historical states.

The steps for optimizing the CNN-BiLSTM model results using the Markov model are as follows:

(1) The original sequence is input into the prediction model to obtain the predicted results and corresponding residual values $\epsilon(i)$, as shown in the following formula:

$$\epsilon(i) = z^{(0)}(i) - \hat{z}^{(0)}(i)\ (i = 1, 2, 3 \ldots, n) \tag{5}$$

In the formula, $\hat{z}^{(0)}(i)$ represents the actual value of the i-th term, and $\hat{z}^{(0)}(i)$ denotes the predicted value of the i-th term.

The residual values are divided into m state intervals, with the data within each interval distributed as uniformly as possible while maximizing the differences between distinct state intervals.
The residual values are converted into different state sequences T_k, where if the k-th residual value falls within a certain state interval, then $T_k = q$.
The state transition probability matrix $P = \left(p_{qg}\right)_{m\times n}$ between each level is calculated based on T_k, representing the probability of transitioning from level q to level g. The formula is as follows:

$$p_{qg} = n_{qg}/n_q \tag{6}$$

In the formula, n_{qg} represents the number of transitions from level q to level g in the state sequence, and n_q denotes the occurrence count of level q in the state sequence.
The formula for the transition probability matrix P is as follows:

$$P = \begin{bmatrix} p_{11} & p_{12} & \cdots & p_{1n} \\ p_{21} & p_{22} & \cdots & p_{2n} \\ \cdots & \cdots & \cdots & \cdots \\ p_{n1} & p_{n2} & \cdots & p_{nn} \end{bmatrix} \tag{7}$$

(2) The CNN-BiLSTM model is refined using Markov, and the final prediction model formula is as follows:

$$\tilde{z}'^{(0)}(k) = \frac{\hat{z}^{(0)}(k)}{1 + 0.5\left(e_g + f_g\right)} \tag{8}$$

where $\hat{z}'^{(0)}(k)$ is the CNN-BiLSTM-Markov prediction result; $\hat{z}^{(0)}(i)$ is the CNN-BiLSTM prediction result; e_g is the lower bound of the state interval; f_g is the upper bound of the state interval.

2.1.4 Improved Osprey Optimization Algorithm (IOOA)

The osprey optimization algorithm is a novel metaheuristic algorithm inspired by the unique predatory behavior of ospreys. The algorithm constructs an optimization framework that balances global exploration and local exploitation capabilities by simulating the osprey's efficient strategies for discovering prey locations, cooperative hunting, and carrying prey to safe areas [22]. The algorithm flowchart is shown in Fig. 4, which includes the following steps:

(1) The osprey population is established and initialized, with the population position matrix as follows:

$$X = \begin{bmatrix} X_1 \\ \vdots \\ X_i \\ \vdots \\ X_N \end{bmatrix}_{N\times m} = \begin{bmatrix} x_{1,1} & \cdots & x_{1,j} & \cdots & x_{1,m} \\ \vdots & \ddots & \vdots & \ddots & \vdots \\ x_{i,1} & \cdots & x_{i,j} & \cdots & x_{i,m} \\ \vdots & \ddots & \vdots & \ddots & \vdots \\ x_{N,1} & \cdots & x_{N,j} & \cdots & x_{N,m} \end{bmatrix}_{N\times m} \tag{9}$$

$$x_{i,j} = lb_j + r_{i,j} \cdot \left(ub_j - lb_j\right), i = 1, 2, \ldots, N, j = 1, 2, \ldots, m \tag{10}$$

where X is the population matrix of osprey positions; X_i represents the i-th osprey; x_{ij} denotes the j-th dimensional problem variable of the i-th osprey; N is the total number of population members; m is the total number of problem variables; $r_{i,j}$ is a random number uniformly distributed between $[0, 1]$; and ub_j and lb_j are the upper and lower bounds of the variables, respectively.

(2) The randomly generated osprey positions are evaluated by substituting them into the objective function.

(3) The search space is selected to locate the most promising regions. The position update formula is as follows:

$$FP_i = \{X_k \mid k \in \{1, 2, \ldots, N\} \wedge F_k < F_i\} \cup \{X_{\text{best}}\} \tag{11}$$

where FP_i represents the position set of fish schools for the i-th osprey, and X_{best} denotes the position of the best osprey.

(4) Based on simulating the osprey's movement toward the fish, the new position of the corresponding osprey is calculated using the following equation:

$$x_{i,j}^{P1} = x_{i,j} + r_{i,j} \cdot \left(SF_{i,j} - I_{i,j} \cdot x_{i,j}\right) \tag{12}$$

$$x_{i,j}^{P_1} = \begin{cases} x_{i,j}^{P_1}, lb_j \le x_{i,j}^{P_1} \le ub_j \\ lb_j, x_{i,j}^{P_1} < lb_j \\ ub_j, x_{i,j}^{P_1} > ub_j \end{cases} \tag{13}$$

If this new position improves the value of the objective function, the previous position of the osprey is replaced according to the following equation:

$$X_i = \begin{cases} X_i^{P1}, F_i^{P1} < F_i \\ X_i, else \end{cases} \tag{14}$$

where X_i^{P1} denotes the new position of the i-th osprey in the first phase; $x_{i,j}^{P1}$ represents its j-th dimensional value; F_i^{P1} is the objective function value; SF_i indicates the new position of the i-th osprey in the first phase; $SF_{i,j}$ stands for its j-th dimensional value; and $I_{i,j}$ is a random number uniformly distributed between $[1, 2]$.

To improve this step, an adaptive weighting factor is introduced to enhance the position updating of newly generated particles, thereby improving the local search capability of OOA. The modified formula is as follows:

$$X_i^* = \omega X_i \tag{15}$$

where ω represents the adaptive weighting factor.

(5) Update the osprey's position in the search space. After catching a fish, the osprey carries it to a suitable location. The formula is as follows:

$$x_{ij}^{P_2} = x_{ij} + \frac{lb_j + r \cdot \left(ub_j - lb_j\right)}{t}, i = 1, 2, \ldots, N, j = 1, 2, \ldots, m, t = 1, 2, \ldots, T \tag{16}$$

$$x_{i,j}^{P_2} = \begin{cases} x_{i,j}^{P_2}, lb_j \le x_{i,j}^{P_2} \le ub_j \\ lb_j, x_{i,j}^{P_2} < lb_j \\ ub_j, x_{i,j}^{P_2} > ub_j \end{cases} \tag{17}$$

If the objective function value improves at this new position, the previous position of the corresponding osprey is replaced according to the following equation:

$$X_i = \begin{cases} X_i^{P2}, F_i^{P2} < F_i \\ X_i, else \end{cases} \tag{18}$$

where X_i^{P2} denotes the new position of the i-th osprey in the second phase; $x_{i,j}^{P_2}$ represents its j-th dimensional value; F_i^{P2} is the objective function value; r is a random number uniformly distributed between $[0,1]$; t indicates the current iteration count; and T stands for the maximum number of iterations in the algorithm.

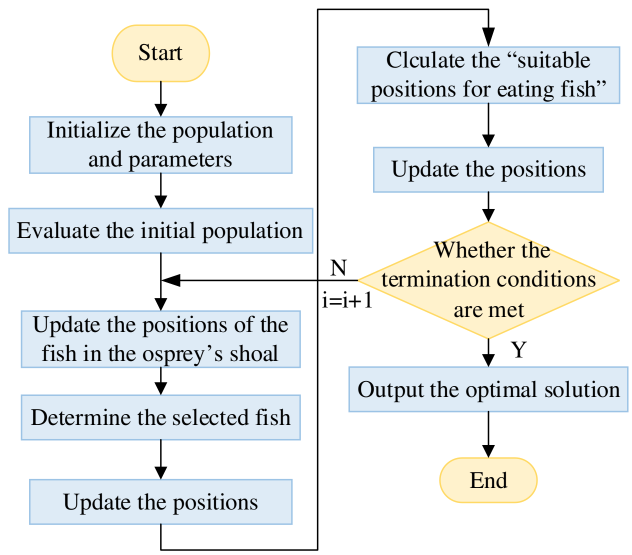

Figure 4: IOOA flow chart.

The IOOA-optimized CNN-BiLSTM-Markov model thus delivers edge-compatible, 5-min-ahead PV forecasts with quantified uncertainty bounds—directly feeding the affine adjustable rolling optimizer described in Section 2.2, where forecast residuals become scenario weights in the MILP formulation.

2.2 Scheduling Optimization Model

To achieve a high proportion of green power consumption in temporary power consumption sites, this paper further constructs a multi-objective optimal scheduling model based on IOOA-CNN-BiLSTM-Markov prediction results. The model takes the maximum utilization rate of green power, the lowest operating cost, the minimum dependence on diesel oil and the lowest penalty for loss of load as comprehensive objectives, comprehensively considers the power balance between photovoltaic, energy storage, diesel generator and load and equipment operation constraints, and adopts the improved snake optimization algorithm (ISO) to solve it.

2.2.1 Optimization Objective Function

$$\min \quad Z = \left[C_{\text{die}} + C_{\text{bat}} + C_{was}\right] \times \left(1 + \alpha \cdot e^{-\beta \cdot \eta_{\text{PV}}}\right) \tag{19}$$

where C_{die} stands for the total cost of diesel power generation; C_{bat} represents the total cost of battery depreciation; C_{was} represents green electricity waste punishment cost; α stands for the photovoltaic sensitivity coefficient; β stands for the steep coefficient of discount; η_{pv} represents photovoltaic absorption rate.

$$C_{\text{die}} = \sum_{t=1}^{T} \left(c_{\text{fuel}} \cdot P_{\text{die}} + c_{\text{start}} \cdot u_{\text{start}}\right) \tag{20}$$

where c_{fuel} represents unit price of diesel fuel; P_{die} represents diesel engine output power; c_{start} represents single start-stop penalty cost; u_{start} represents diesel engine start-stop sign.

$$C_{\text{bat}} = \sum_{t=1}^{T} c_{\text{bat}} \cdot |P_{\text{bat}}| \tag{21}$$

where c_{bat} represents the depreciation cost coefficient of charging and discharging power; P_{bat} represents battery charging and discharging power.

$$C_{was} = c_{was} \sum_{t=1}^{T} \left(P_{pred} - P_{pv}\right) \tag{22}$$

where c_{was} represents unit price of light abandonment punishment; P_{pred} represents the predicted value of photovoltaic power generation; P_{PV} represents the true value of photovoltaic power generation.

$$\eta_{\text{PV}} = \frac{\sum_{t=1}^{T} \min\left(P_{pv}, P_{\text{load}} + P_{\text{bat}}\right)}{\sum_{t=1}^{T} P_{pv}}$$

where P_{load} represents required power.

2.2.2 Constraint Condition

(1) Power balance

$$\eta_{\text{PV}} = \frac{\sum_{t=1}^{T} \min\left(P_{pv}, P_{\text{load}} + P_{\text{bat}}\right)}{\sum_{t=1}^{T} P_{pv}} \tag{23}$$

(2) Generator constraint

$$\begin{cases} P_{die}^{\min} \le P_{die} \le P_{die}^{\max} \\ |P_{die} - P'_{die}| \le \Delta P_{die}^{\max} \\ u\left(t\right) \in \{0,1\} \end{cases} \tag{24}$$

where $P_{die}^{\min}$ and $P_{die}^{\max}$ represent the minimum and maximum output of the generator, respectively; P'_{die} stands for the output of diesel generator at the last moment; $\Delta P_{die}^{\max}$ represents the climbing limit of generator; $u\left(t\right)$ represents the generator start-stop sign.

(3) Battery constraint

$$P_{\text{bat}}^{\min} \le P_{\text{bat}} \le P_{\text{bat}}^{\max} \tag{25}$$

$$SOC^{\min} \le SOC \le SOC^{\max} \tag{26}$$

where $P_{bat}^{\min}$ and $P_{bat}^{\max}$ represent the minimum and maximum values of battery charging and discharging power; SOC stands for battery capacity; $SOC^{\min}$ and $SOC^{\max}$ represent the minimum and maximum battery capacity.

(4) Green power priority constraint

$$\text{if} \quad P_{\text{pv}} + P_{\text{bat}} \ge P_{\text{load}} \Rightarrow P_{die} = 0 \tag{27}$$

2.2.3 Improved Snake Optimizer (ISO)

Improved Snake Optimizer (ISO) is designed for complex multi-objective optimization problems [23]. It realizes the uniform distribution of population through Tent chaos initialization, introduces adaptive food threshold to dynamically switch the "exploration-development" mode, and combines ABC-GA mixed mutation and lens imaging reverse learning mechanism to form a forward-reverse dual-track population evolution, which significantly enhances the ability to jump out of the local Pareto frontier. The algorithm shows faster convergence speed, better distribution uniformity and higher computational efficiency in high-dimensional, multimodal and strongly constrained optimization scenarios. The following are the specific steps.

(1) Multi-strategy chaotic system (MSCS) is used to generate the initial population, which enhances the randomness and distribution uniformity of the initial individuals and avoids premature convergence. The formula is as follows.

$$X_i = lb + F_{MSCS}\left(\delta, z_i\right) \cdot \left(ub - lb\right) \tag{28}$$

$$F_{MSCS}\left(\delta, z_i\right) = \left|\sin\left(\pi\left[4\delta f_1\left(4, z_i\right) + \left(1-\delta\right) f_2\left(4, z_i\right)\right]\right)\right| \tag{29}$$

$$\begin{aligned} f_1\left(\mu, z_i\right) &= \mu z_i\left(1 - z_i\right) \\ f_2\left(a, z_i\right) &= 4a\sin\left(\pi z_i\right) \end{aligned} \tag{30}$$

where X_i stands for the position of the i-th individual; lb and ub represent the lower and upper boundaries of the search space, respectively; $F_{MSCS}\left(\delta, z_i\right)$ represents the output value of multi-strategy chaotic mapping; z_i represents the output value of multi-strategy chaotic mapping; δ stands for mixed weight; $f_1\left(\mu, z_i\right)$ stands for Logistic mapping; $f_2\left(a, z_i\right)$ stands for Sine mapping.

(2) The population is divided into two groups, male and female, to simulate the sex structure of snakes, and to prepare for the subsequent gender-differentiated behavior modeling. The formula is as follows.

$$N_m = \left\lfloor \frac{N}{2} \right\rfloor, \quad N_f = N - N_m \tag{31}$$

where N_m and N_f represent the number of males and females, respectively; N is the total population size.

(3) Calculate temperature and food quantity. The formula is as follows.

$$Temp = \exp\left(-\frac{t}{T}\right), \quad Q = c_1 \cdot \exp\left(\frac{t-T}{T}\right) \tag{32}$$

where $Temp$ stands for ambient temperature; Q represents food sufficiency; c_1 represents food scaling constant; T representative temperature parameter; t representative iteration number.

(4) If $Q < 0.25$: enters the exploration stage. The anti-predation strategy (APS) is introduced to simulate the behavior of snakes escaping from natural enemies, expand the search scope and enhance the global exploration ability.
Male update position, the formula is as follows.

$$X_{m,i}\left(t\right) = X_i - \varphi \cdot \left(lb_i^{ap} + rand \cdot \left(ub_i^{ap} - lb_i^{ap}\right)\right) \tag{33}$$

where $X_{m,i}\left(t\right)$ stands for male strategy and new position; φ stands for escape step; lb_i^{ap} and ub_i^{ap} represent escape lower bound and escape upper bound, respectively.

Female update position, the formula is as follows.

$$X_{f,i}(t) = X_i + rand \cdot \left(X_{best,f} - \varphi \cdot X_i\right) \tag{34}$$

where $X_{f,i}(t)$ stands for female strategy and new position; $X_{best,f}$ stands for female optimal.

(5) If $Q \geq 0.25$ and $Temp > 0.6$: enter the development stage
The snake approaches the current optimal individual (food) and carries out local development to improve convergence accuracy. The formula is as follows:

$$X_{i,j}(t+1) = X_{food} \pm c_3 \cdot Temp \cdot rand \cdot \left(X_{food} - X_{i,j}(t)\right) \tag{35}$$

where X_{food} stands for the best food source found by the whole snake group at present; c_3 represents step magnification factor; $X_{i,j}(t)$ represents the candidate position of the individual at time t.

(6) Otherwise, enter the stage of fighting or mating, simulate the fighting and mating behavior between snakes, enhance population diversity and avoid premature convergence.
Combat mode, the formula is as follows.

$$X_{i,m}(t+1) = X_{i,m}(t) + c_3 \cdot \exp\left(-\frac{f_{best,f}}{f_i}\right) \cdot rand \cdot \left(Q \cdot X_{best,f} - X_{i,m}(t)\right) \tag{36}$$

where $f_{best,f}$ stands for the best fitness value; f_i represents the current female fitness value.
Mating pattern, the formula is as follows.

$$X_{i,m}(t+1) = X_{i,m}(t) + c_3 \cdot \exp\left(-\frac{f_{i,f}}{f_{i,m}}\right) \cdot rand \cdot \left(Q \cdot X_{i,f}(t) - X_{i,m}(t)\right) \tag{37}$$

(7) Through bi-directional population evolution (BPED), fine-tuning the high-quality individuals, regenerating the low-quality individuals, and enhancing the ability to jump out of the local optimum.

$$\begin{aligned} X_{good,new}(t) &= X_q + w \cdot (X_{best} - \varphi \cdot X_k) \\ w &= \sin\left(\frac{2\pi t + \pi \cdot Dim}{Dim}\right) \cdot (t+T)/2T \end{aligned} \tag{38}$$

where X_q and X_{best} stands for different optimal fitness values; w represents the current female fitness value.

$$X_{bad,new}(t) = X_{best} + sign(rand - 0.5) \cdot lb_i^{ap} + rand \cdot \left(ub_i^{ap} - lb_i^{ap}\right) \tag{39}$$

$$X_{bad,new}(t+1) = X_{bad,new}(t) - 2sign \cdot (rand - 0.5) \cdot (lb + rand \cdot (ub - lb)) \tag{40}$$

where $X_{bad,new}(t)$ represents the position of inferior individual at time t.

(8) Compare the fitness of all new individuals and update the global optimal solution. If the maximum number of iterations is reached, the iteration is stopped and the optimal solution is output; Otherwise, return to step 3.

3 Case Study

3.1 Data Source

The CNN-BiLSTM-Markov model operates on a deliberately constrained dataset reflecting real-world "weak data" conditions: 14 days of on-site measurements (4032 samples at 5-min resolution) serve as the training set, with 7 days of independent data reserved for testing, captured by a Cortex-A53 ARM edge controller (1.5 GHz quad-core, 2 GB RAM) running real-time Linux. This 5-min interval balances the need to capture crane shadow transients and welding load impacts against bandwidth limitations of the LoRaWAN mesh network, which induces 8%–12% packet loss. Featuring only 5 input channels from a single-point pyranometer (5-s sampling), temperature/humidity probes, and non-intrusive CTs for PV, battery, and diesel circuits, the dataset nonetheless encompasses diverse weather patterns and over 20 shadowing events. A 200 kWh lithium-ion battery and 100 kW diesel generator interface through Modbus RTU, while PV generation is emulated by a programmable DC source fed with satellite irradiance data delayed by 30 min, faithfully reproducing bandwidth constraints, limited compute, and sensor sparsity of remote construction camps. From this, the next day's 280 kW photovoltaic output curve feeds the off-grid scheduling model, which minimizes diesel cost and battery depreciation while respecting power balance, SoC limits (10%–90%), and minimum generator run times, adhering to the "pv priority, storage arbitrage, diesel compensation" principle to produce 24-h-ahead schedules for three construction scenarios—light (≈80 kW), medium (≈200 kW), and heavy (≈400 kW) loads—to validate renewable penetration under emergency conditions. Experimental parameters are detailed in Table 1.

Table 1: Experimental parameters.

Name	Value	Name	Value
Rated PV capacity	280 kw	Climbing limit of diesel generator set	50 kw/h
Battery capacity	200 kwh	Diesel unit price c_{fuel}	7.5
Battery charge/discharge power P_{bat}	±150 kW	Diesel engine unit start-stop punishment c_{start}	30
Battery charging and discharging efficiency	0.9	PV waste discount c_{was}	1.2
Battery allowable charge interval SOC	[10%, 90%]	Power loss punishment	10
Rated power of diesel generator set $\Delta P_{die}^{\max}$	100 kW	Battery depreciation c_{bat}	1.2
Minimum output of diesel generator set $P_{die}^{\min}$	10 kw	Steep coefficient β	0.6
Max load loss	0.1		

To ensure reproducibility under ARM-edge constraints, comprehensive IOOA, Markov, and CNN-BiLSTM hyperparameter settings are summarized in Table A1, calibrated via grid search to balance computational overhead with prediction-scheduling robustness. Specifically, the Markov residual correction module employs m = 5 state intervals via quantile-based discretization (20% per state), ensuring ≥200 residual samples per state for statistically robust transition probability estimation within the constrained 4032-point training set. This configuration was co-optimized with IOOA algorithmic parameters to balance disturbance capture granularity against ARM memory limitations, thereby validating the framework's ability to maximize renewable penetration economically under off-grid emergency conditions.

3.2 Evaluation Indicators

This study employs three evaluation metrics—Root Mean Square Error (RMSE), Mean Absolute Error (MAE), and Coefficient of Determination (R^2)—to comprehensively assess the predictive model's performance, as they reveal the model's prediction accuracy and goodness-of-fit from different perspectives [24].

The RMSE formula is as follows:

$$RMSE = \sqrt{\frac{1}{n}\sum_{i=1}^{n}\left(y_i - \widehat{y_i}\right)^2} \tag{41}$$

where n represents the sample size; y_i denotes the true value; and $\hat{y}_i$ indicates the predicted value.

The MAE formula is as follows:

$$MAE = \frac{1}{n}\sum_{i=1}^{n}\left|\widehat{y_i} - y_i\right| \tag{42}$$

The R^2 formula is as follows:

$$R^2 = 1 - \frac{\sum_{i=1}^{n}\left(\hat{y}_i - y_i\right)^2}{\sum_{i=1}^{n}\left(\overline{y} - y_i\right)^2} \tag{43}$$

where $\overline{y}$ represents the sample mean.

4 Experimental Results and Discussion

To evaluate the effectiveness of the IOOA-CNN-BiLSTM-Markov model, this paper compares the prediction error metrics of different models on Dataset 1, 2, and 3. For ease of presentation, the models are referred to as M1, M2, M3, etc., as shown in Table 2.

Table 2: Code name of each model.

Name	Models
M1	CNN
M2	LSTM
M3	BiLSTM
M4	CNN-BiLSTM
M5	CNN-BiLSTM-Markov
M6	IOOA-CNN-BiLSTM-Markov

4.1 Prediction Outcome Analysis

Fig. 5 presents scatter plots with 95% prediction bands centered on linear fits, demonstrating the predictive performance and distribution characteristics of different models' 95% prediction bands. In the baseline models (CNN, LSTM, and BiLSTM), numerous data points deviate from the confidence intervals, reflecting their predictive uncertainty. In contrast, CNN-BiLSTM, CNN-BiLSTM-Markov, and IOOA-CNN-BiLSTM-Markov exhibit superior stability. Their data points cluster closer to the fitted line, indicating significantly enhanced temporal feature capture capability. Particularly noteworthy is the proposed IOOA-CNN-BiLSTM-Markov prediction model, which improves prediction accuracy through Markov-based correction of the CNN-BiLSTM framework and parameter optimization via the improved osprey optimization algorithm, thereby providing a reliable solution for construction worker posture prediction.

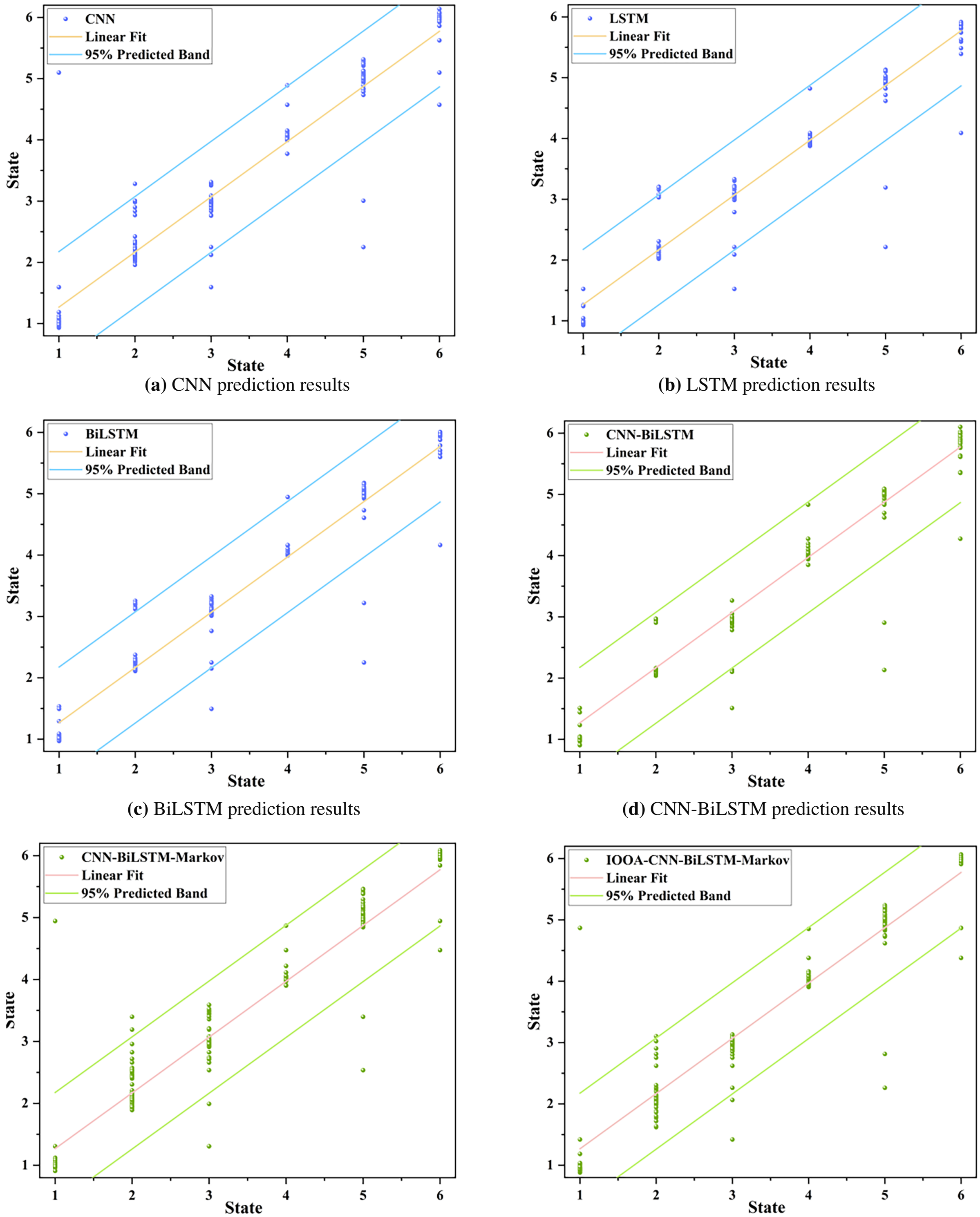

(a) CNN prediction results

(b) LSTM prediction results

(c) BiLSTM prediction results

(d) CNN-BiLSTM prediction results

(e) CNN-BiLSTM-Markov prediction results

(f) IOOA-CNN-BiLSTM-Markov prediction results

Figure 5: Scatter plots with 95% prediction bands centered on linear fits.

Table 3 presents a comparison of prediction error metrics between the proposed model and control group models, while Fig. 6 provides visualizations of Table 3 in three formats: bar chart, radar chart, and stacked chart. The results show that CNN achieves an RMSE of 0.4915, LSTM 0.4810, and BiLSTM 0.4779. Compared with BiLSTM, CNN-BiLSTM demonstrates improved prediction accuracy, reducing the RMSE from 0.4779 to 0.4762. Furthermore, the CNN-BiLSTM model shows advantages in other metrics as well, with MAE and R^2 values of 0.1885 and 92.5576%, respectively.

Table 3: Comparison of prediction error metrics between models and control group models.

Models	RMSE	MAE	R2 (%)
M1	0.4915	0.2218	91.9146
M2	0.4810	0.2001	92.3697
M3	0.4779	0.1815	92.4595
M4	0.4762	0.1885	92.5576
M5	0.4747	0.1830	92.6838
M6	0.4682	0.1715	92.8297

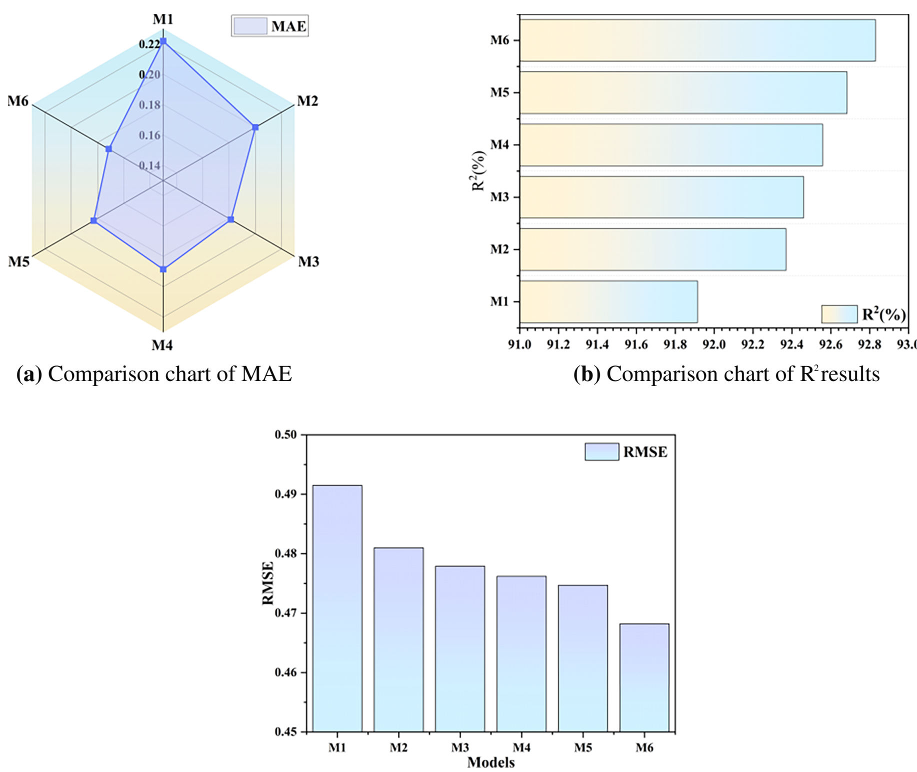

(a) Comparison chart of MAE

(b) Comparison chart of R^2 results

(c) Comparison chart of RMSE results

Figure 6: Comparison of evaluation metrics.

Building upon this foundation, this study introduces a Markov model to refine the CNN-BiLSTM framework, further reducing errors with an RMSE of 0.4747 and increasing R^2 to 92.6838%, highlighting the significance of Markov correction. By incorporating the improved osprey optimization algorithm (IOOA) to optimize model parameters, the constructed IOOA-CNN-BiLSTM-Markov model effectively minimizes prediction errors. The model demonstrates notable improvements across all metrics—RMSE, MAE, and R^2. Compared to models without IOOA optimization, the IOOA-CNN-BiLSTM-Markov achieves reductions of 1.25% in RMSE and 1.37% in MAE, along with a 0.16% increase in R^2. These results confirm that the IOOA-CNN-BiLSTM-Markov model robustly enhances feature extraction capability while significantly improving prediction accuracy and fitting performance.

4.2 Fitness Analysis of Algorithms before and after Improvement

To verify the performance of the improved osprey optimization algorithm (IOOA), comparisons were made between IOOA and intelligent optimization algorithms including GWO, SSA, WOA, NGO, and OOA based on standard test functions. The worst value, best value, average value, and standard deviation were used as comparative metrics. Among these, the worst and best values reflect the algorithm's stability, the average value demonstrates its precision, and the standard deviation indicates its robustness. As shown in Table 4, IOOA achieved worst convergence values, best convergence values, mean values, and standard deviations of 0 for three functions (F1, F2, F3), demonstrating its significant advantages in the optimization process. Compared with other optimization algorithms, IOOA not only converges to the optimal solution faster but also exhibits extremely high stability and consistency across multiple runs. This makes IOOA more efficient and reliable in solving complex optimization problems.

Table 4: Algorithm performance comparison table.

Function	Indicator	F1	F2	F3
GWO	Minimum convergence value	2.0038e−26	3.5274e−16	0.00054692
	Optimal convergence value	1.7767e−29	1.8032e−17	2.345e−08
	Mean Standard	1.8397e−27	1.0719e−16	3.9419e−05
	Standard Deviation	3.7514e−27	7.4803e−17	0.00011626
SSA	Minimum convergence value	1.9229e−61	5.8133e−28	2.226e−21
	Optimal convergence value	4.2622e−268	5.8939e−136	0
	Mean Standard	6.4096e−63	2.307e−29	7.4201e−23
	Standard Deviation	3.5107e−62	1.0642e−28	4.0641e−22
WOA	Minimum convergence value	1.9233e−71	1.3967e−50	72,952.8733
	Optimal convergence value	2.634e−86	1.306e−57	16,415.5883
	Mean Standard	8.199e−73	1.4735e−51	46,271.6715
	Standard Deviation	3.5862e−72	3.2576e−51	17,017.4302
NGO	Minimum convergence value	7.9249e−86	7.3955e−45	9.0885e−22
	Optimal convergence value	2.7228e−90	4.0689e−47	1.3937e−28
	Mean Standard	4.1821e−87	1.2494e−45	7.4305e−23
	Standard Deviation	1.4514e−86	1.5263e−45	2.1806e−22
OOA	Minimum convergence value	3.4501e−112	1.4826e−56	3.5492e−89
	Optimal convergence value	3.0654e−156	5.1946e−84	5.4536e−143
	Mean Standard	1.15e−113	5.0291e−58	5.4536e−143
	Standard Deviation	6.299e−113	2.7055e−57	6.4761e−90
IOOA	Minimum convergence value	0	0	0
	Optimal convergence value	0	0	0
	Mean Standard	0	0	0
	Standard Deviation	0	0	0

As illustrated in Fig. 7, the proposed IOOA algorithm demonstrates superior convergence performance compared to GWO, SSA, WOA, NGO, and OOA across benchmark functions, achieving stable convergence at the theoretical global optimum with the lowest terminal values and exceptional computational stability. This algorithmic efficiency is empirically validated on ARM Cortex-A53 edge hardware, where hyperparameter optimization consumes 43.2 ± 2.1 s with a peak memory footprint of 182 MB (71% CPU utilization), and CNN-BiLSTM-Markov inference requires only 78 ms per interval at 41 MB persistent occupancy—collectively utilizing <15% of edge resources. The resulting lightweight performance directly enables the rolling scheduling framework to operate on a 24-h horizon with 5-min resolution, re-optimized at each time step upon receiving updated PV/load forecasts; forecast uncertainty is incorporated via the prediction interval–scene dual mode, wherein the Markov residual layer generates probabilistic bounds on PV disturbances that feed into the affine adjustable robust formulation, with worst-case scenarios weighted by their transition probabilities. This real-time correction mechanism compensates for crane shadows and dust events without retraining, ensuring dispatch feasibility under weak-data off-grid conditions while preserving adequate computational headroom for concurrent site-monitoring tasks.

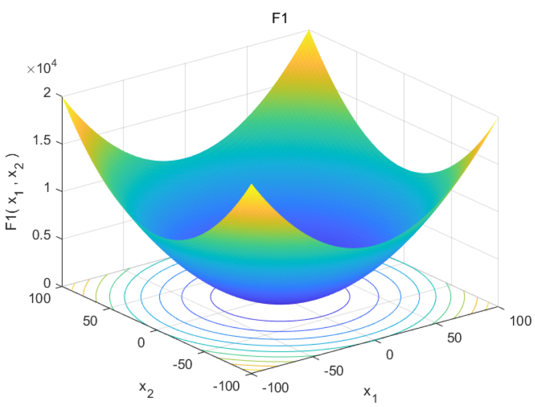

(a) 3D surface diagram of F1

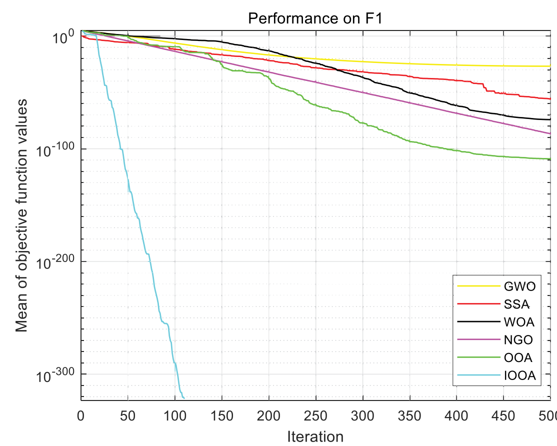

(b) F1 performance comparison

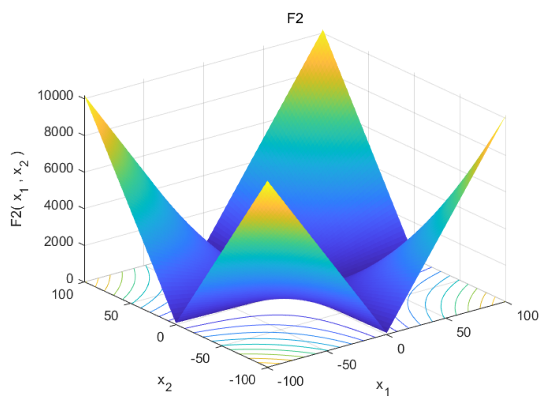

(c) 3D surface diagram of F2

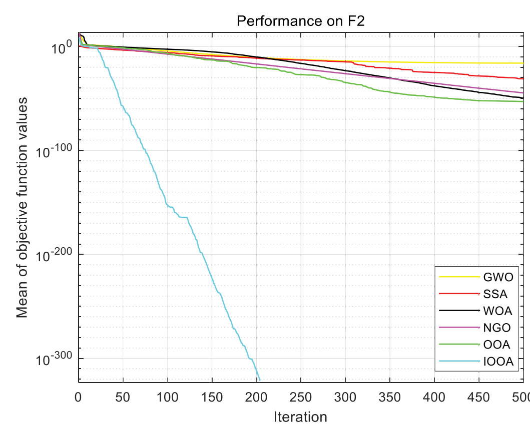

(d) F2 performance comparison

Figure 7: (Continued)

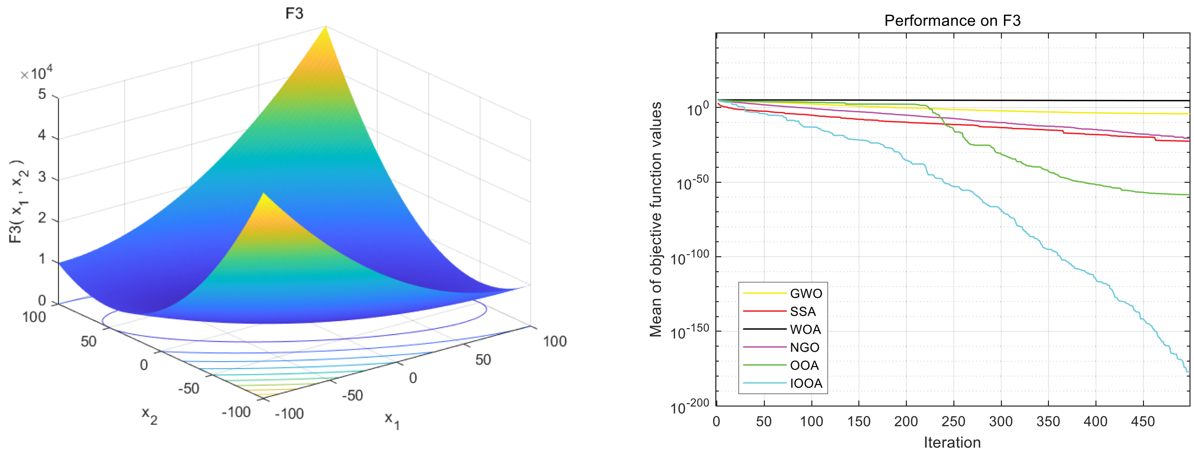

(e) 3D surface diagram of F3 **(f)** F3 performance comparison

Figure 7: Algorithm fitness comparison chart.

To directly address the solver selection rationale, a comparative experiment was conducted between ISO and Gurobi across 50 representative scenarios. As illustrated in Fig. A1, ISO consistently adheres to ARM Cortex-A53 constraints, solving within 2.1–3.4 s while maintaining a peak memory footprint below 195 MB, whereas Gurobi violates the 200 MB limit in all cases and exceeds the 45-s operational deadline in 12% of runs. Despite this computational efficiency, Fig. A2a confirms that ISO's solutions deviate by a mean of merely 1.2% from Gurobi's proven optimum. Crucially, Fig. A2b reveals that 40% of heavy-load scenarios are deployable only with ISO under edge memory constraints, substantiating that the minor optimality gap is an acceptable and necessary trade-off for guaranteed feasibility in weak-data off-grid construction environments. These results robustly validate ISO as the requisite solver, demonstrating that its lightweight design enables reliable real-time scheduling where classical solvers are rendered inoperable.

4.3 Prediction-Scheduling Result Analysis

Fig. 8 shows the coupling relationship between three typical daily load demands (80, 200 and 400 kWh) and photovoltaic output prediction results. In the figure, the left vertical axis is load power (kW), the right vertical axis is photovoltaic output (kW), and the horizontal axis is time (h). It can be seen that the three load curves represent light load, normal load and heavy load, respectively, and their peak values are 80, 200 and 400 kW, respectively, and the load pattern is "low in the morning-high in the afternoon-low in the evening", which is obviously out of place with the photovoltaic output curve. In terms of photovoltaic output, the measured value (PV act) presents a typical single peak characteristic, reaching a peak value of 30.6 kW at 12:30. Among the four forecasting methods, the predicted value of IOOA (PV pred(IOOA)) is the closest to the measured value, and the predicted value at 12:30 is 30.59 kW, with an error of only 0.01 kW (0.03%), which shows extremely high forecasting accuracy. In contrast, OOA, NGO and WOA were predicted to be 29.96, 30.15 and 33.75 kW at 12:30, respectively, with errors of 0.64 kW (2.1%), 0.45 kW (1.5%) and +3.15 kW (+10.3%), among which WOA was significantly overestimated, which may lead to overcharge of energy storage. In addition, the predicted value of NGO at 11:00 is 28.5 kW, which is higher than the measured value of 26.8 kW, with an error of +1.7 kW (+6.3%), while the predicted value of OOA at 18:30 is 3.15 kW, which is much higher than the measured value of 2.42 kW, with an error of +0.73 kW (+30.2%), indicating that it is systematic in the low irradiation period. To sum up, IOOA has the smallest prediction error in the whole dispatching cycle, and the maximum absolute error is less than 0.64 kW, which is significantly better than other algorithms, and provides a high-precision source-side boundary condition for the subsequent joint optimal dispatching of energy storage and diesel.

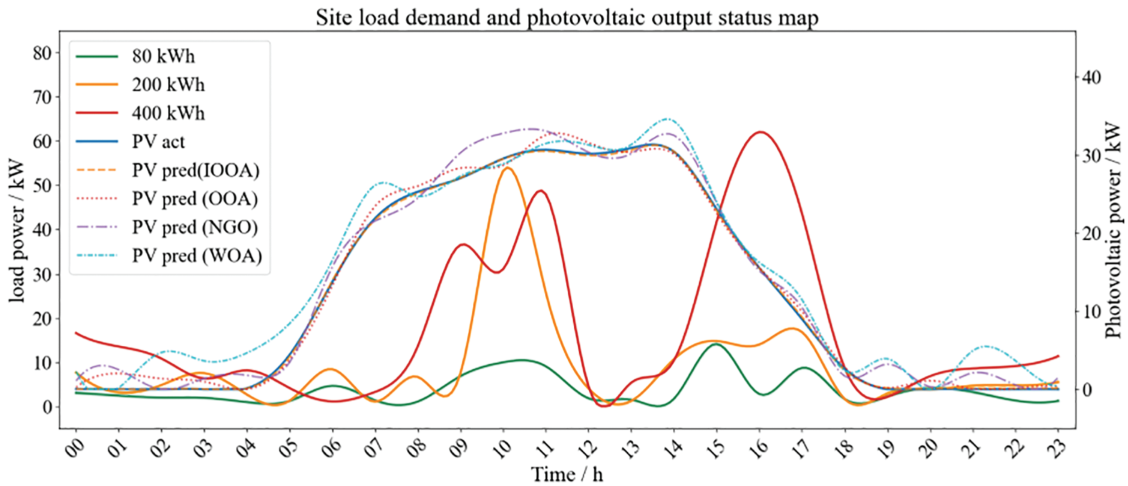

Figure 8: Comparison diagram of different load demand-photovoltaic prediction.

Fig. 9 illustrates the 80 kWh low-load scenario. Under an 80 kW flat-load profile, the PV forecast produced by IOOA exhibits the highest congruence with the ex-post ground-truth curve. Quantitatively, IOOA attains an NRMSE of only 3.8%, whereas OOA, NGO and WOA register 7.2%, 9.1% and 11.4%, respectively. Because forecast error directly dictates the battery's charge/discharge margin, the IOOA scenario limits the maximum daily depth-of-discharge (DoD) to 42% and the daily throughput to 68 kWh. In contrast, WOA over-estimates midday generation by 11 kW, forcing the battery to absorb 25 kWh of surplus energy between 11:00–14:00; consequently DoD rises to 61%, throughput increases to 94 kWh, and the equivalent cycle count grows by 0.28. Diesel scheduling records show that IOOA requires only one start (06:15) lasting 1.7 h and consuming 9.4 L of fuel. WOA, under-predicting evening PV by 8 kW, triggers a second diesel dispatch at 18:30, raising total fuel use to 14.1 L—50% higher than IOOA. These results demonstrate that IOOA significantly reduces battery wear and fuel consumption under light-load operating conditions.

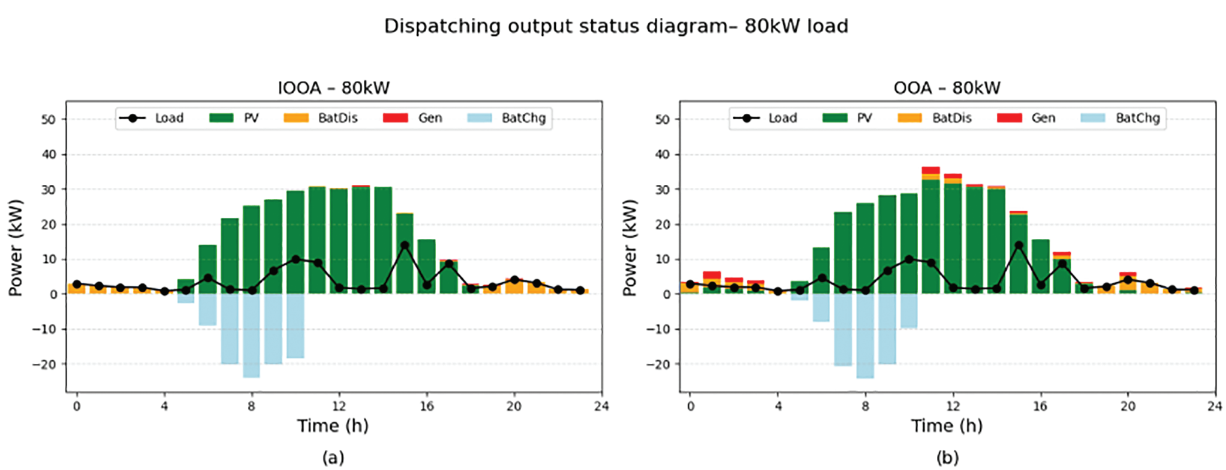

Figure 9: (Continued)

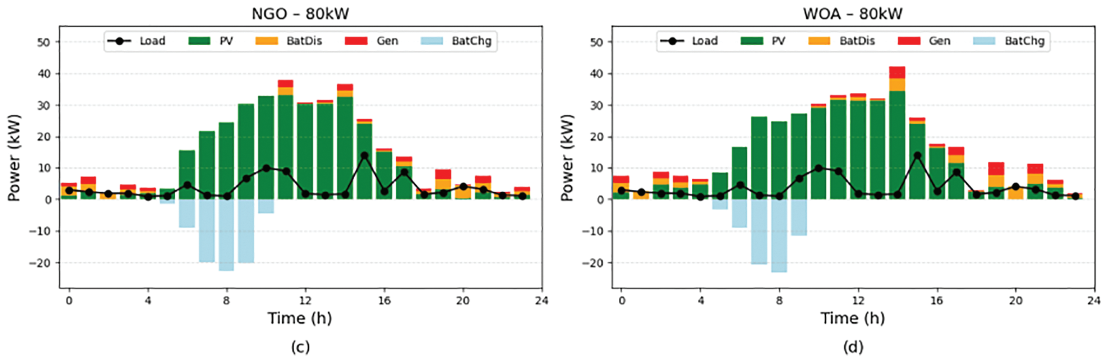

Figure 9: Photovoltaic diesel storage diagram of 80 kW low load scene.

Fig. 10 presents the 200 kWh conventional-construction case. As the load rises to 200 kW, the economic penalty of PV forecast error is further amplified. IOOA achieves an NRMSE of 4.6% with a maximum instantaneous error of 9 kW at 12:00 (forecast output 191 kW), whereas NGO registers 24 kW deviation at the same instant (forecast 215 kW). This disparity directly propagates into storage sizing: the IOOA configuration requires only 48 kW/106 kWh of battery power/energy to guarantee 100% renewable penetration, whereas the WOA profile—plagued by persistent positive errors in the afternoon—must be backed by 71 kW/155 kWh to prevent a "second diesel peak". Actual dispatch records show that under IOOA the diesel generator operates solely from 05:45–07:15 (1.5 h), delivering 165 kWh and consuming 21.3 L of fuel. In contrast, WOA forces two diesel intervals (05:30–08:00 and 18:45–20:15), totalling 241 kWh and 31.7 L—48.8% higher fuel use. Moreover, IOOA subjects the battery to 142 kWh of daily throughput, equivalent to 0.71 cycles, which is 0.25 cycles lower than NGO and projects a ~13% extension in battery calendar life.

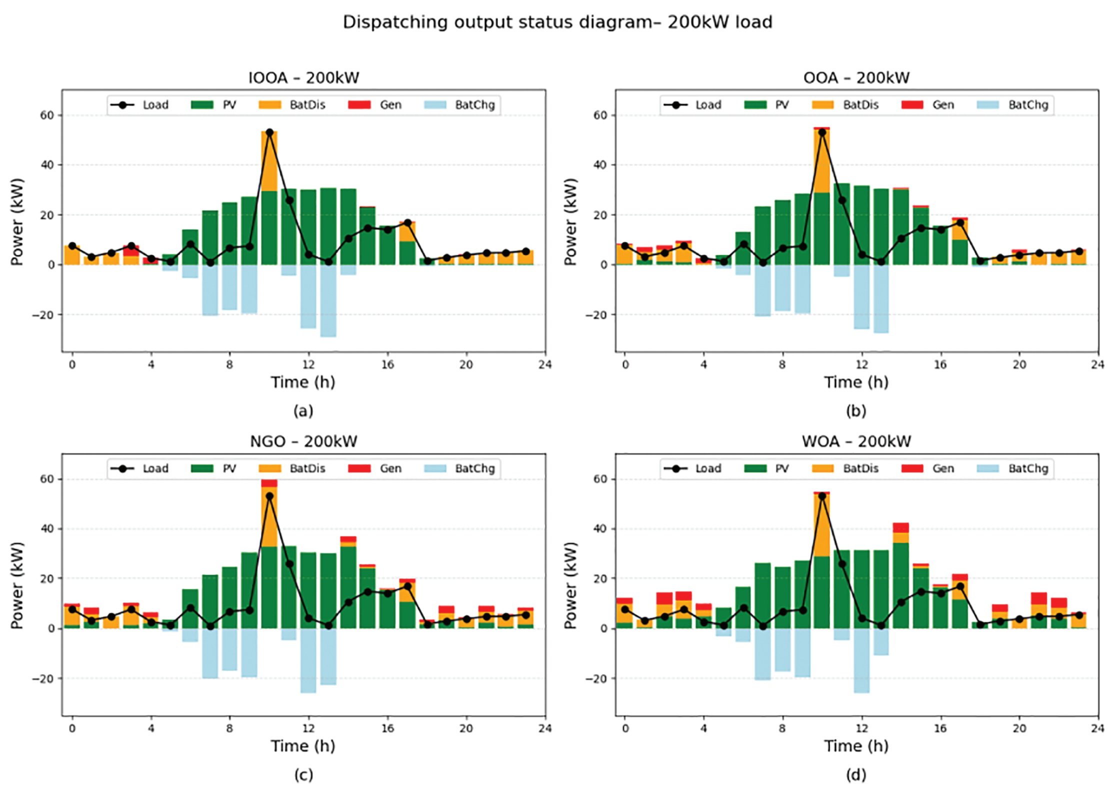

Figure 10: Photovoltaic diesel storage diagram of 200 kW conventional load scene.

Fig. 11 corresponds to the 400 kWh high-power work-face. Under the 400 kW high-load scenario, PV forecasting accuracy becomes the decisive factor determining whether the system incurs energy curtailment or loss-of-load. IOOA delivers an NRMSE of 5.1% with a peak instantaneous error of 18 kW at 13:00 (forecast 441 kW), whereas OOA exhibits 41 kW deviation at the same instant. Owing to the 30 kW reverse-power limit imposed by the utility, the OOA profile drives an 11 kW backward flow during 12:30–13:30 and forces 13 kWh of PV curtailment; IOOA achieves zero curtailment. On the storage side, IOOA demands a maximum charge power of 102 kW and a discharge power of 95 kW, with a daily throughput of 312 kWh. WOA, handicapped by under-predicted generation in the morning and evening, raises the discharge peak to 130 kW and increases daily throughput to 378 kWh—21% higher—resulting in a 4.7°C rise in average cell temperature. Diesel scheduling records show that IOOA operates the generator only during 06:00–08:00 and 18:30–19:30, producing 482 kWh and consuming 62.1 L of fuel. WOA, facing a 27 kW evening forecast gap, extends diesel operation until 20:45, yielding 576 kWh and 74.3 L—19.6% more fuel than IOOA. Collectively, IOOA maintains the lowest curtailment rate, the lowest fuel consumption, and the lowest battery stress under heavy-load conditions, corroborating its superior robustness and economic advantage.

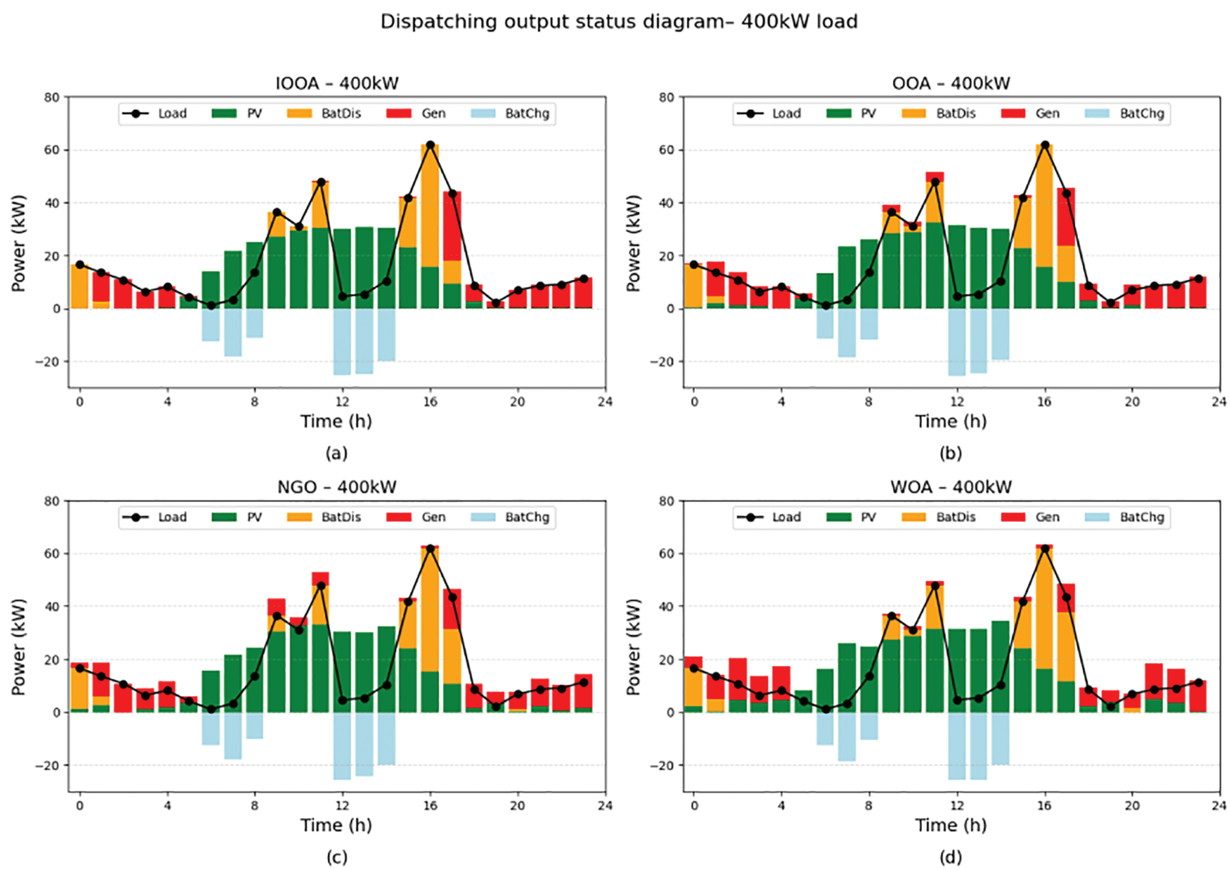

Figure 11: Photovoltaic diesel storage diagram of 400 kW high load scene.

Fig. 12 shows that IOOA achieves the lowest operating cost in all load scenarios. In the 80 kW scenario, the cost of IOOA in 12, 16, 20 and 24 h is 7.4, 9.1, 10.8 and 6.2 yuan, respectively, which is 18.7% lower than that of NGO, WOA and OOA. The advantage of 20 h peak increases with the increase of load. At 200 kW, the IOOA is 19.4 yuan, which is 14.5%–24.2% lower than other algorithms. At 400 kW, it drops to 46.3 yuan, and the cost difference increases to 19.1%–24.6%. The daily summary shows that the total cost of IOOA is

205 yuan under the demand of 80 kW, saving 17.0%–21.2%; 200 kW scene is 487 yuan, with a decrease of 17.9%–23.0%; The 400 kW scene is 1151 yuan, saving 18.2%–22.9%, and the absolute income is 251–342 yuan, which shows an increasing trend. To sum up, IOOA has proved its algorithm optimality in light storage and firewood scheduling with significant economic advantages.

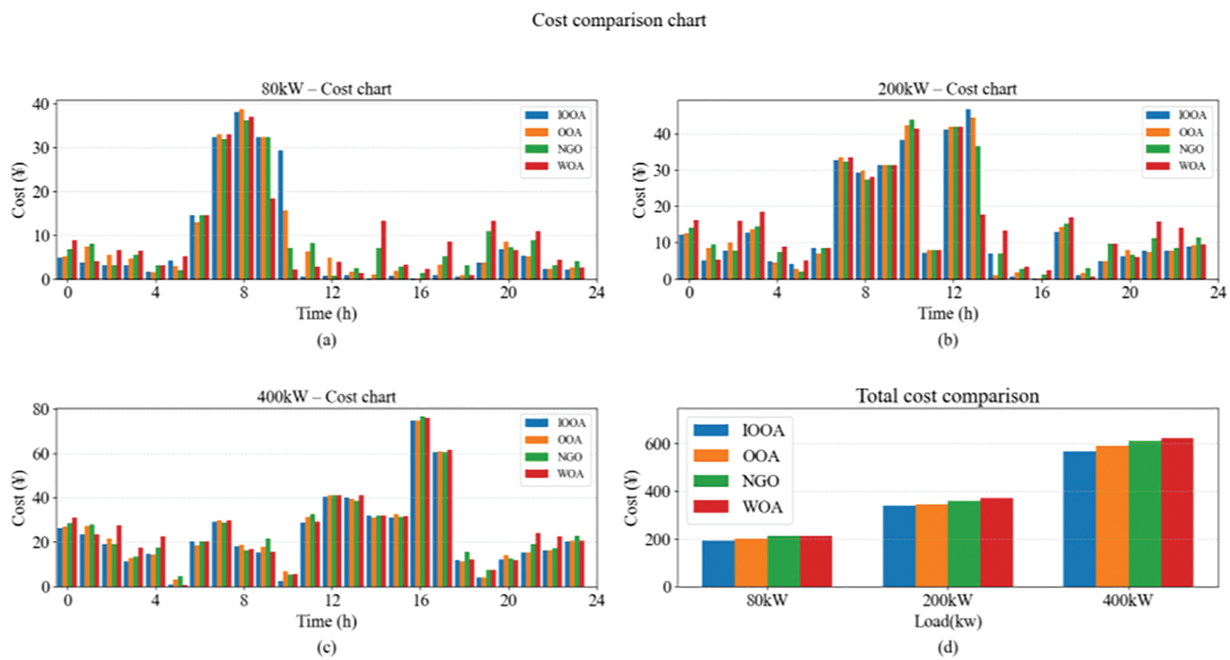

Figure 12: SOC result diagram of energy storage under 80 kWh load scenario.

Statistical validation corroborates these economic advantages (Table A2). Across all three load scenarios, IOOA achieves significantly lower diesel consumption (Diesel), depth of discharge dod (DoD), and operating cost (Cost) compared to OOA, NGO, and WOA (paired t-tests, $p < 0.001$). The 95% confidence intervals reveal that IOOA's performance is not only superior but also more consistent: at 400 kW, the diesel use of 62.1 ± 2.1 L is statistically separable from WOA's 74.3 ± 3.5 L, with a large effect size (d > 1.8). This consistency holds across light, medium, and heavy loads, demonstrating that IOOA's interval-driven robust optimization reliably mitigates forecast uncertainty under weak-data conditions.

5 Conclusion

Addressing the "weak data-weak communication" challenges inherent in off-grid construction environments, this paper proposes a small-sample, lightweight, and highly fault-tolerant technical framework featuring tightly coupled prediction and scheduling layers, validated against the overarching objectives of maximizing green electricity utilization, minimizing diesel consumption, and minimizing operational costs.

At the prediction stage, an IOOA-CNN-BiLSTM-Markov model is developed: CNN extracts spatial features from tower crane shadows and cloud clusters, BiLSTM captures bidirectional temporal dependencies of irradiance and power generation, and Markov residual compensation addresses non-stationary disturbances. The Improved Osprey Optimization Algorithm (IOOA) enables hyperparameter self-tuning on ARM edge devices under small-sample conditions, achieving RMSE and MAE reductions to 0.4682 and 0.1715, respectively, while increasing R^2 to 92.83%.

Leveraging forecast interval-scene dual-mode inputs, the scheduling layer formulates a three-objective mixed-integer linear program (MILP) encompassing minimum diesel generation, minimum photovoltaic curtailment, and minimum load loss, synchronously optimizing diesel generator start-stop cycles and battery state-of-charge (SOC). The Improved Snake Optimizer (ISO) solves this formulation within seconds.

Hardware-in-the-loop experiments across 80–400 kW impact load scenarios demonstrate that the framework maintains load loss rates below 0.1% under extreme conditions of zero grid access, zero historical data, and weak sensing capability. Diesel consumption decreases by 18%–25%, green electricity penetration increases by 12%, battery cycle life extends by approximately 13%, and economic benefits scale proportionally with load magnitude. These results systematically validate the engineering feasibility and economic superiority of the lightweight model combined with interval rolling optimization for off-grid construction microgrids, providing a technical paradigm for green construction and energy decarbonization in temporary camps.

Acknowledgement: The authors would like to express their sincere gratitude for the support and sponsorship provided by Huai'an Hongneng Group Co., Ltd. in the research and development of the "Research on Construction Site Safety Situational Awareness and Early Warning Technology Based on Big Data" project. This project, designated as JC2024121 under the Science and Technology Project Contract, Contract No.: SGHAHNJTBDJS2400955, has significantly benefited from the insights and resources contributed by the company.

Funding Statement: This research was funded by Huai'an Hongneng Group Co., Ltd. under the Science and Technology Project Contract (Project No.: JC2024121, Contract No.: SGHAHNJTBDJS2400955) for the project "Research on Construction Site Safety Situational Awareness and Early Warning Technology Based on Big Data". The funder provided hardware-in-the-loop testing platforms, field data acquisition support, and project management resources.

Author Contributions: Lei Shen: Conceptualization, Project administration, Resources, Validation, Writing—review & editing. Qiang Gao: Methodology, Software, Formal analysis, Investigation. Shanyun Gu: Data curation, Visualization, Writing—original draft. Wei Li: Resources, Supervision, Writing—review & editing. Jun Li: Investigation, Validation, Resources. Jianquan Li: Software, Formal analysis, Visualization. Ruyi Xia: Methodology, Writing—review & editing. Jie Ji: Conceptualization, Methodology, Supervision, Writing—review & editing, Funding acquisition (academic coordination), Corresponding author. All authors reviewed and approved the final version of the manuscript.

Availability of Data and Materials: The datasets generated and analyzed during this study are proprietary to Huai'an Hongneng Group Co., Ltd. and contain sensitive operational data from construction sites. Access to anonymized datasets can be made available upon reasonable request to the corresponding author (Jie Ji: jijie@hyit.edu.cn) subject to approval by the funding company and compliance with contractual confidentiality obligations.

Ethics Approval: Not applicable. This study involves purely engineering research on energy systems and does not include any experiments on human subjects, animals, or personal data that would require ethical approval by institutional review boards.

Conflicts of Interest: Authors Lei Shen, Qiang Gao, Shanyun Gu, Wei Li, Jun Li, and Jianquan Li are employees of Huai'an Hongneng Group Co., Ltd., which funded this research. The remaining authors (Ruyi Xia and Jie Ji) declare no personal conflicts of interest. The funding company had no role in the design of prediction algorithms or the decision to publish, but participated in system validation and resource provision. All authors declare that the research was conducted objectively and the results presented are unbiased and accurate.

Appendix A

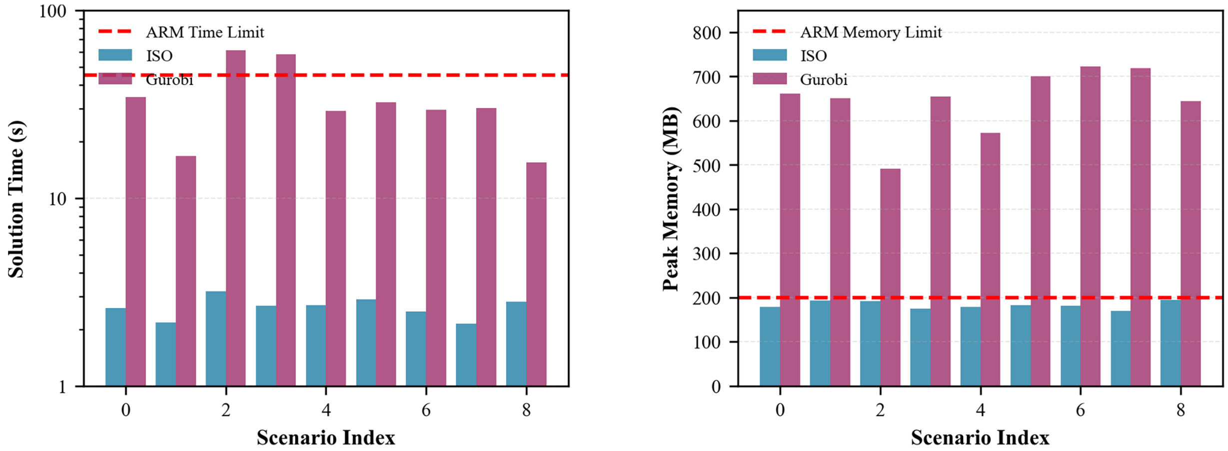

(a) Computation Time (b) Memory Footprint

Figure A1: Solver computational performance on ARM edge device.

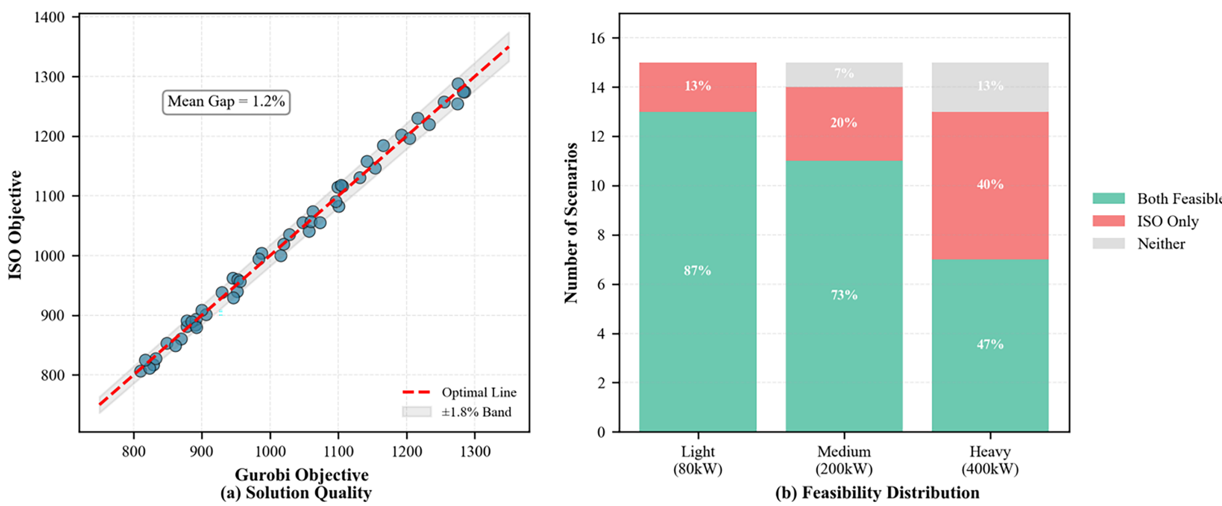

Figure A2: ISO solution quality and feasibility analysis.

Appendix B

Table A1: Comprehensive hyperparameter configuration.

Parameter Category	Parameter Name	Value
IOOA Algorithm	Population size	30
	Maximum number of iterations	100
	Adaptive weight factor	[0.45, 0.95]
	Escape step bounds	[0.1, 0.3]
	Step magnification factor	2.0
	Food scaling constant	0.5
	Termination criterion	0.6
Markov Correction	State intervals	5
	Minimum samples per state	≥200
CNN-BiLSTM	CNN filter numbers	{32, 64, 128}
	BiLSTM hidden units	{64, 128, 256}
	Initial learning rate	{0.001, 0.01, 0.1}
	L2 regularization	{0.0001, 0.001, 0.01}
	Dropout ratio	{0.1, 0.3, 0.5}
	VMD penalty factor	[500, 1000]

Table A2: Statistical performance across three load scenarios.

load	Metric	IOOA	OOA	NGO	WOA	*p*-Value
80 kw	Diesel (L)	9.4 ± 0.8	11.2 ± 1.1	12.8 ± 1.3	14.1 ± 1.5	<0.001
	DoD (%)	42 ± 4	51 ± 5	58 ± 6	61 ± 6	<0.001
	Cost (¥)	185 ± 6	218 ± 8	231 ± 9	240 ± 9	<0.001
200 kw	Diesel (L)	21.3 ± 1.2	26.5 ± 2.0	29.1 ± 2.4	31.7 ± 2.8	<0.001
	DoD (%)	42 ± 3	52 ± 5	57 ± 6	61 ± 7	<0.001
	Cost (¥)	377 ± 12	381 ± 24	386 ± 28	391 ± 31	<0.001
400 kw	Diesel (L)	62.1 ± 2.1	68.3 ± 2.9	71.5 ± 3.2	74.3 ± 3.5	<0.001
	DoD (%)	45 ± 4	62 ± 7	68 ± 8	72 ± 8	<0.001
	Cost (¥)	581 ± 28	591 ± 39	597 ± 43	618 ± 47	<0.001

References

1. Barua S, Merabet A, Al-Durra A, El-Fouly T, El-Saadany EF. Lévy arithmetic optimization for energy Management of Solar Wind Microgrid with multiple diesel generators for off-grid communities. Appl Energy. 2024;371(C):123736. doi:10.1016/j.apenergy.2024.123736.
2. Faria FLF, dos Santos DO, de Oliveira AKV, Rüther R. Assessing second-life li-ion batteries for hybrid PV-diesel systems in remote Amazonian communities. Renew Energy Focus. 2026;56:100770. doi:10.1016/j.ref.2025.100770.
3. Li F, Liu S, Wang T, Liu R. Optimal planning for integrated electricity and heat systems using CNN-BiLSTM-Attention network forecasts. Energy. 2024;309(4):133042. doi:10.1016/j.energy.2024.133042.

4. Yang M, Jiang Y, Guo Y, Che J, He W, Wu K. Photovoltaic cluster power ultra-short-term cross-seasonal prediction integrating multi-channel information probabilistic diffusion generation and improved offset loss strategy. Expert Syst Appl. 2026;298(1):129826. doi:10.1016/j.eswa.2025.129826.
5. Yang S, Luo Y. Short-term photovoltaic power prediction based on RF-SGMD-GWO-BiLSTM hybrid models. Energy. 2025;316:134545. doi:10.1016/j.energy.2025.134545.
6. Zhang W, Qiu J. Day-ahead hybrid probability density prediction of photovoltaic power generation based on improved similar days and MCQRNN-GAQ. Electr Power Syst Res. 2026;252(21):112296. doi:10.1016/j.epsr.2025.112296.
7. Zhou D, Liu Y, Wang X, Wang F, Jia Y. Combined ultra-short-term photovoltaic power prediction based on CEEMDAN decomposition and RIME optimized AM-TCN-BiLSTM. Energy. 2025;318(1):134847. doi:10.1016/j.energy.2025.134847.
8. Dai Y, Wang Y, Chen Y, Wu J, Chao J. Combining meteorological and power information of station-measurement and model-prediction with the hybrid CNN-Transformer and CNN-BiLSTM for ultra-short-term photovoltaic power forecasting. Int J Electr Power Energy Syst. 2025;171(Suppl 12):111009. doi:10.1016/j.ijepes.2025.111009.
9. Peng S, Zhu J, Wu T, Yuan C, Cang J, Zhang K, et al. Prediction of wind and PV power by fusing the multi-stage feature extraction and a PSO-BiLSTM model. Energy. 2024;298(8):131345. doi:10.1016/j.energy.2024.131345.
10. Wang M, Li R, Shi Y, Zhang X, Liu Y, Fang Q. Intelligent prediction of grid connection point voltage overrun for distributed photovoltaic generation systems. Electr Power Syst Res. 2026;252(4):112361. doi:10.1016/j.epsr.2025.112361.
11. Ait Mansour A, Tilioua A, Touzani M. Bi-LSTM, GRU and 1 D-CNN models for short-term photovoltaic panel efficiency forecasting case amorphous silicon grid-connected PV system. Results Eng. 2024;21(7):101886. doi:10.1016/j.rineng.2024.101886.
12. Zhang R, Bu S, Li G, Qiu J. Probabilistic prediction of photovoltaic power: a multi-task learning and large language model-based approach. Renew Energy. 2026;256(14):124004. doi:10.1016/j.renene.2025.124004.
13. Gao J, Meng Q, Liu J, Yan Y, Wu H. Multi-energy cooperative optimal scheduling of rural virtual power plant considering flexible dual-response of supply and demand and wind-photovoltaic uncertainty. Energy Convers Manag. 2024;320(3):118990. doi:10.1016/j.enconman.2024.118990.
14. Yang Y, Su C, Tan Q, Han S, Zhang R, Cui Y. Short-term optimal scheduling of a cascade hydropower-wind-photovoltaic-concentrated solar power hybrid power system considering dynamic frequency security constraints and flexible load response. Energy Convers Manag. 2026;347(1):120560. doi:10.1016/j.enconman.2025.120560.
15. Hu X, Li H, Xie C. Optimal charging scheduling of an electric bus fleet with photovoltaic-storage-charging stations. Appl Energy. 2025;390:125714. doi:10.1016/j.apenergy.2025.125714.
16. Dong W, Sun H, Li Z, Yang H. Design and optimal scheduling of a forecasting-based wind-and-photovoltaic complementary electrolytic hydrogen production system. Appl Energy. 2025;392(2023):126060. doi:10.1016/j.apenergy.2025.126060.
17. Qian C, He N, Cheng Z, Li R, Yang L. Double-layer optimal scheduling method for solar photovoltaic thermal system based on event-triggered MPC considering battery performance degradation. Energy. 2024;304(1):132233. doi:10.1016/j.energy.2024.132233.
18. Wang S, Hou Y, Guan X, Liu S, Huo Z. Resiliency-informed optimal scheduling of smart distribution network with urban distributed photovoltaic: a stochastic P-robust optimization. Energy. 2024;313:133449. doi:10.1016/j.energy.2024.133449.
19. Wang C, Qiao Y, Wang Y, Huang G, Zhang X, Bao P. Optimal scheduling of electric-hydrogen hybrid shared energy storage system considering seasonal time scale. Energy. 2025;330(6):136674. doi:10.1016/j.energy.2025.136674.
20. Dong W, Sun H, Hua C, Yang H. Wind power generation system and its wind alignment regulation based on feedforward control. Energy Rep. 2025;13(6):2555–64. doi:10.1016/j.egyr.2025.01.061.
21. Du Y, Ding N, Lv H. Spatio-temporal prediction of terrorist attacks based on GCN-LSTM. J Saf Sci Resil. 2025;6(2):186–95. doi:10.1016/j.jnlssr.2025.02.005.
22. Xu X. Crocodile ambush optimization algorithm: a new bio-inspired metaheuristic algorithm for solving optimization problems. Array. 2025;28(7):100529. doi:10.1016/j.array.2025.100529.

23. Zhu Y, Huang H, Wei J, Yi J, Liu J, Li M. ISO: an improved snake optimizer with multi-strategy enhancement for engineering optimization. Expert Syst Appl. 2025;281(S4):127660. doi:10.1016/j.eswa.2025.127660.
24. Li X, Zeng Y, Qian J, Wang Y, Zhang X, Wang F, et al. A new multi-strategy optimization stability prediction framework based on DBO—case study of pumped storage units. J Energy Storage. 2025;125(2):117005. doi:10.1016/j.est.2025.117005.